Resolving power of diffraction imaging with an objective: a numerical study

WENJIN WANG,[1,2] JING LIU,[1,3] JUN QING LU,[4,1] JUNHUA DING,[5,1] AND XIN-HUA HU[4,1,*]

[1]*Institute for Advanced Optics, Hunan Institute of Science and Technology, Yueyang, Hunan 414006, China*
[2]*School of Physics, Hunan Institute of Science and Technology, Yueyang, Hunan 414006, China*
[3]*School of Information, Hunan Institute of Science and Technology, Yueyang, Hunan 414006, China*
[4]*Department of Physics, East Carolina University, Greenville, NC 27858, USA*
[5]*Department of Computer Science, East Carolina University, Greenville, NC 27858, USA*
**hux@ecu.edu*

Abstract: Diffraction imaging in far-field can detect 3D morphological features of an object for its coherent nature. We describe methods for accurate calculation and analysis of diffraction images of scatterers of single and double spheres by an imaging unit based on microscope objective at non-conjugate positions. Quantitative study of the calculated diffraction imaging in spectral domain has been performed to assess the resolving power of diffraction imaging. It has been shown numerically that with coherent illumination of 532nm in wavelength the imaging unit can resolve single spheres of 2μm or larger in diameters and double spheres separated by less than 300nm between their centers.

OCIS codes: (110.0180) Microscopy, (110.1650) Coherence imaging, (100.2960) Image analysis.

References and links

1. G. C. Salzman, S. B. Singham, R. G. Johnston, and C. F. Bohren, "Light scattering and cytometry," in *Flow Cytometry and Sorting*, M. R. Melamed, T. Lindmo, and M. L. Mendelsohn, eds. (Wiley, New York, 1990), Ch. 5.
2. A. Wax, C. Yang, V. Backman, K. Badizadegan, C. W. Boone, R. R. Dasari, and M. S. Feld, "Cellular organization and substructure measured using angle-resolved low-coherence interferometry," Biophys. J. **82**, 2256-2264 (2002).
3. M. M. Hanczyc, S. M. Fujikawa, and J. W. Szostak, "Experimental models of primitive cellular compartments: encapsulation, growth, and division," Science **302**, 618-622 (2003).
4. K. V. Gilev, M. A. Yurkin, E. S. Chernyshova, D. I. Strokotov, A. V. Chernyshev, and V. P. Maltsev, "Mature red blood cells: from optical model to inverse light-scattering problem," Biomed. Opt. Express **7**, 1305-1310 (2016).
5. M. Bessis, and N. Mohandas, "A diffractometric method for the measurement of cellular deformability," Blood cells **1**, 307-313 (1975).
6. S. Holler, Y. Pan, R. K. Chang, J. R. Bottiger, S. C. Hill, and D. B. Hillis, "Two-dimensional angular optical scattering for the characterization of airborne microparticles," Opt. Lett. **23**, 1489-1491 (1998).
7. J. Neukammer, C. Gohlke, A. Hope, T. Wessel, and H. Rinneberg, "Angular distribution of light scattered by single biological cells and oriented particle agglomerates," Appl. Opt. **42**, 6388-6397 (2003).
8. X. Su, S. E. Kirkwood, M. Gupta, L. Marquez-Curtis, Y. Qiu, A. Janowska-Wieczorek, W. Rozmus, and Y. Y. Tsui, "Microscope-based label-free microfluidic cytometry," Opt. Express **19**, 387-398 (2011).
9. K. M. Jacobs, L. V. Yang, J. Ding, A. E. Ekpenyong, R. Castellone, J. Q. Lu, and X. H. Hu, "Diffraction imaging of spheres and melanoma cells with a microscope objective," J. Biophotonics **2**, 521–527 (2009).
10. K. M. Jacobs, J. Q. Lu, and X. H. Hu, "Development of a diffraction imaging flow cytometer," Opt. Lett. **34**, 2985-2987 (2009).
11. K. Dong, Y. Feng, K. M. Jacobs, J. Q. Lu, R. S. Brock, L. V. Yang, F. E. Bertrand, M. A. Farwell, and X. H. Hu, "Label-free classification of cultured cells through diffraction imaging," Biomed. Opt. Express **2**, 1717-1726 (2011).
12. Y. Sa, J. Zhang, M. S. Moran, J. Q. Lu, Y. Feng, and X. H. Hu, "A novel method of diffraction imaging flow cytometry for sizing microspheres," Opt. Express **20**, 22245–22251 (2012).
13. Y. Feng, N. Zhang, K. M. Jacobs, W. Jiang, L. V. Yang, Z. Li, J. Zhang, J. Q. Lu, and X. H. Hu, "Polarization imaging and classification of Jurkat T and Ramos B cells using a flow cytometer," Cytometry A **85**, 817-826 (2014).

14. R. Pan, Y. Feng, Y. Sa, J. Q. Lu, K. M. Jacobs, and X. H. Hu, "Analysis of diffraction imaging in non-conjugate configurations," Opt. Express **22**, 31568–31574 (2014).
15. J. Zhang, Y. Feng, W. Jiang, J. Q. Lu, Y. Sa, J. Ding, and X. H. Hu, "Realistic optical cell modeling and diffraction imaging simulation for study of optical and morphological parameters of nucleus," Opt. Express **24**, 366-377 (2016).
16. M. Portnoff, "Time-frequency representation of digital signals and systems based on short-time Fourier analysis," IEEE T. Acous. Speech Signal Proces. **28**, 55-69 (1980).
17. M. A. Yurkin, and A. G. Hoekstra, "The discrete-dipole-approximation code ADDA: capabilities and known limitations," J. Quant. Spectrosc. Radiat. Transfer **112**, 2234-2247 (2011).
18. H. Wang, Y. Feng, Y. Sa, Y. Ma, R. Pan, J. Q. Lu, and X. H. Hu, "Acquisition of cross-polarized diffraction images and study of blurring effect by one time-delay-integration camera," Appl. Opt. **54**, 5223-5228 (2015).
19. X. Ma, J. Q. Lu, R. S. Brock, K. M. Jacobs, P. Yang, and X. H. Hu, "Determination of complex refractive index of polystyrene microspheres from 370 to 1610 nm," Phys. Med. Biol. **48**, 4165-4172 (2003).
20. P. Zhang, P. M. Goodwin, and J. H. Werner, "Fast, super resolution imaging via Bessel-beam stimulated emission depletion microscopy," Opt. Express **22**, 12398-12409 (2014).

1. Introduction

Angle-resolved study of elastically scattered light in far-field led to various tools for assay of micrometer-sized particles including biological cells by the contrast mechanism based on the 3D heterogeneity in refractive index (RI) [1-4]. In comparison, imaging of coherent light scatter has been much less explored for the challenges to acquire and assess high-contrast images [5-8]. In recent years, we have developed a diffraction imaging flow cytometry (DIFC) method for measurement of high-contrast images from micrometer-sized particles carried by a laminar flow through the focus of an incident laser beam [9-13]. The essential design of DIFC imaging unit contains an infinity-corrected microscope objective of 0.55 in numerical aperture (NA), a tube lens and an imaging sensor placed at its focal plane Γ_{im} as illustrated in Fig. 1(A). Previously we have developed and validated a method for accurate simulation of diffraction imaging process combining a vector wave model on light scattering and a geometric model for tracing the "rays" through the imaging unit [14, 15]. The new method can reproduce the diffraction images (DIs) measured at non-conjugate positions by varying angular cone of light detection for enhanced image contrast. This variability, however, makes it difficult to determine the resolving power of DIFC because no analytical relations exist between field-of-view (FOV) and scatterer's morphology at a non-conjugate position. In this report we describe and apply a method based on the short-time-Fourier-transform (STFT) algorithm [12, 16] for analyzing DIs and finding the ability of the imaging unit to resolve small morphological variations in a scatterer made of two spheres, which is similar to the approach for deriving the Abbe and Rayleigh criterions on resolving two objects except that the spheres are connected in 3D space.

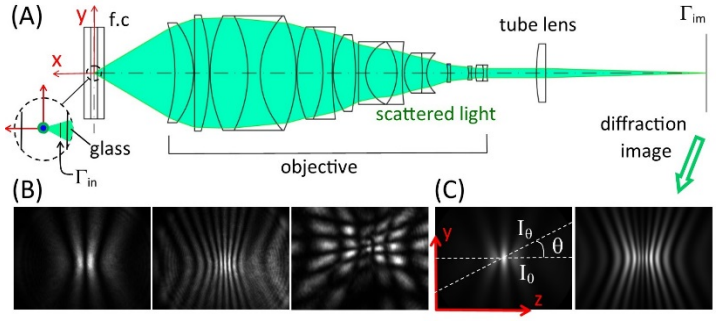

Fig. 1. (A) Configuration of the DIFC system for DI measurement and simulations with an incident beam of λ=532nm propagating along z-axis (into paper): f.ch.=flow chamber; (B) measured DIs of single spheres in water with nominal diameter value of d=2.5μm (left), 7.9μm (center) and two spheres of d=5.7μm (right) at Δx=150μm; (C) calculated DI of single sphere in water with d=2.5μm (left) and 7.9μm (right) as I(y, z), n_{sr}=1.588, n_{si}=3.5x10^{-4}, λ=532nm, n_h=1.334 and Δx=150μm, dash lines indicated sampled lines I_θ in Eq. (1).

2. Method

It has been shown experimentally and numerically that the imaging unit for DI acquisition can record similar patterns of fringes or speckle distribution with the unit translated to an off-focus position by $\Delta x > 0$ [9, 10, 14]. Positive Δx corresponds to moving the unit, including its sensor at Γ_{im}, towards scatterer from a focusing position, which is defined as the location with Γ_{im} conjugate to the plane of scatterer at the flow chamber center. Changing Δx varies the angular cone for DI acquisition and allows for contrast and FOV optimization [14]. Examples of measured and calculated DIs of 640x480 pixels are presented in Fig. 1(B), 1(C), Fig. 3 and Fig. 4 with Δx set to 150 μm. One can match easily the measured DIs with calculated ones exhibiting high resemblance for scatterers of single and double spheres. We ignored the effect of CCD noise in consideration of resolution here since the measured DIs are of high contrast with dark current noise less than 0.2% of full scale in sensor's 12-bit pixel output.

Calculation of DIs consists of three steps as elucidated by Fig. 1(A). First, a scatterer is defined by its 3D distribution of complex RI as $n_s(\mathbf{r}, \lambda) = n_{sr}(\mathbf{r}, \lambda) + in_{si}(\mathbf{r}, \lambda)$ with λ as the incident light wavelength. Elastic light scattering is modeled by a method of discrete dipole approximation (DDA) using a plane wavefield for the incident beam. We chose an open-source software ADDA which imports $n_s(\mathbf{r}, \lambda)$ in a host medium of n_h to obtain the Mueller matrix of elements $S_{ij}(\theta_s, \phi_s)$ for calculation of scattered light intensities of different polarization attributes [4, 17], where i or j=1, 2, 3 4 and θ_s and ϕ_s are respectively the polar and azimuthal angles of scattered light "rays". For simplicity, we limit analysis here to calculation of unpolarized DIs by $S_{11}(\theta_s, \phi_s)$. Extension to polarized DIs is straightforward using other elements [15, 18]. In the second step, the scattered light intensity proportional to $S_{11}(\theta_s, \phi_s)$ is projected to an input plane Γ_{in} defined in Fig. 1(A). Γ_{in} is in the host medium of water with θ_{wm} as the maximum cone angle from the x-axis for light detection and details of projecting S_{11} to Γ_{in} were described elsewhere [11]. Finally, DI is calculated by ray-tracing each pixel in the input image at Γ_{in} along a direction defined by (θ_s, ϕ_s) through a virtual imaging unit with the same design as the one in our DIFC system to produce I(z, y) at Γ_{im} using a commercial ray-tracing software (Zemax, 2009). The ADDA based DI calculation for single spheres has been validated against Mie based results as described in [14] and measured DIs acquired with our DIFC system. All computations except ADDA and Zemax were performed with in-house codes built on MATLAB ((MathWorks, 2013a). The ADDA simulations were carried out with value of dpl (dipoles per wavelength) set to 20 and the values of RI for spheres and host medium chose as those of polystyrene and water for λ=532nm [19].

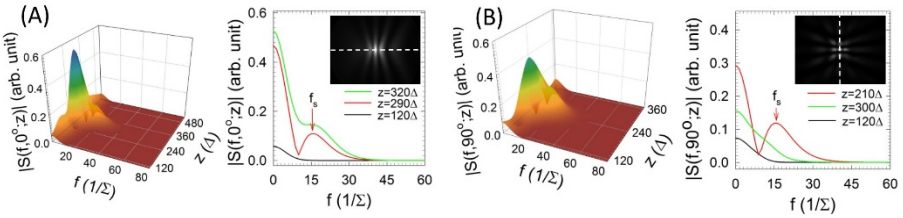

Fig. 2. The STFT power spectra $|S(f, \theta; z)|$ performed on a line I_θ sampled at θ from a calculated DI (insets with dash lines) for different scatterers versus f and z in unit of pixel distance Δ: (A) a single sphere of d=3.00μm and θ=0°; (B) two spheres of connection vector **C** with (010) as direction and $|\mathbf{C}|$=d, θ=90°. DI simulation parameters are given by n_{sr}=1.588, $n_{si}=3.5\text{x}10^{-4}$, λ=532nm, n_h=1.334, Δx=150μm, dpl=20.

For this study, we set out to quantitatively analyze the ability of DI on resolving morphological changes in scatterers of high symmetry or I(z, y) with oscillation in brightness. The STFT algorithm has been extended to transform I(z, y) into S(f, θ) in a 2D domain of frequency and angle. First, a pixel line I_θ is sampled from I(z, y) at an angle θ from the z-axis

as illustrated in Fig. 1(C) followed by Fourier transform on I_θ after multiplication by a Gaussian window of width w. These operations can be described in continuous form as [16]

$$S(f,\theta;z)=\int_0^{\Sigma'} I_\theta(z')\exp\{-\frac{\pi(z'-z)^2}{w^2}\}\exp\{-2\pi ifz'\}dz', \quad (1)$$

where Σ' is the FOV over $I_\theta(z)=I(z, y)$ with $y=y_c+(z-z_c)\tan\theta$ and (y_c, z_c) are the center coordinates of I. After tests with different window width, we fixed w at 3 times of the mean pixel distances of major peaks in I_θ that yields optimized spatial and spectral resolutions. A clear sideband peak at frequency f_s can be identified in $|S(f, \theta; z)|$ of DI containing oscillating patterns with this choice of w. Fig. 2 presents two examples of |S|. Comparisons to STFT on parallel lines of I(z, y) and 2D Gabor transform show that Eq. (1) provides an effective way to identify a single sideband peak for characterizing local oscillations of different orientations.

3. Results

3.1 Single spheres

With $2\theta_{wm}=46.4^o$ as determined by the choice of Δx=150mm [14], DIs of single sphere were calculated with d ranging from 1.0 to 8.5μm with step of 0.5 μm. These results serve as the baseline data for extraction of parameters from the STFT spectra to characterize the oscillating patterns with varying periods. As shown in Fig. 3, diffraction images of spheres with d = 1.0 and 1.5μm contain no oscillating patterns due to the finite value of θ_{wm} and thus no sideband can be observed in |S|. In comparison, as d increases to 2.0 μm and above, a sideband appears clearly in $|S(f, \theta; z)|$ for estimating d value of the sphere from the peak frequency f_s. Since the fringe patterns in DIs displayed in Fig. 3(A) are symmetric to the horizontal direction, we present in Figs. 3(B) and (C) only the STFT spectra on lines sampled at θ=0.

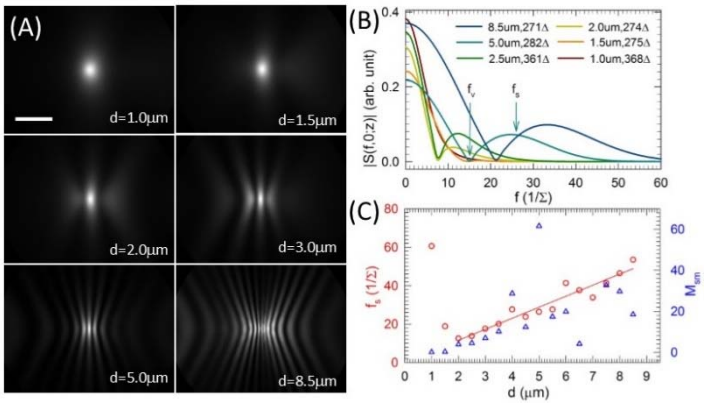

Fig. 3. (A) Calculated DIs of single spheres with different diameter d as marked, bar=10° in detection angle in water; (B) $|S(f, 0^o; z)|$ of calculated DIs in (A) at z of maximum M_s with legends showing d and z (in unit of pixel size Δ) values, f_v and f_s are indicated by the arrows for the case of d=5.0μm; (C) f_s and M_{sm} obtained from DIs versus d, the solid line is a straight line fitted to f_s with $M_{sm} > 1$. Other parameters are the same as those in Fig. 2.

Due to the local nature of brightness oscillation in I_θ, sidebands exist only in STFT spectra of sampled lines windowed at certain z's. As the Gaussian window slides on I_θ, f_s varies near the middle of the line and disappear at the ends. A figure of merit $M_s(\theta,z)$ is defined for evaluation of existence and sharpness of a sideband in $|S(f,\theta; z)|$ as follows

$$M_s(\theta,z)=\frac{|S(f_s,\theta;z)|}{|S(0,\theta;z)|}\frac{|S(f_s,\theta;z)|}{|S(f_v,\theta;z)|}, \quad (2)$$

where f_v is the frequency of the minimum or valley between the DC component of f=0 and f_s. In cases of $f_v > f_s$, a sideband does exist and $|S(f_v, \theta; z)|$ in the denominator of $M_s(\theta, z)$ is set to $|S(0, \theta; z)|$. Fig. 3(B) plots the STFT spectra at the value of z with maximum M_s, denoted as $M_{sm}(\theta=0)$ for selected single spheres and indicate the frequencies of f_s and f_v for the case of d=5.0μm. In addition to selecting z as the best window center for determining f_s, M_{sm} and associated f_s can be used together as a compressed expression of the STFT spectra for line I_θ sampled from I(z, y) since $M_{sm} < 1$ if I_θ has no sidebands. Both f_s and M_{sm} are plotted in Fig. 3(C) to demonstrate a linear relation as expected between f_s and d despite small variations due to the sensitivity of STFT to the variation of w and brightness [12] and other ADDA simulation parameters. It should be pointed out that the objective based imaging unit could increase its ability to recognize single spheres of diameters less than 2.0μm with smaller Δx or λ. But this capability is limited by the objective's NA.

3.2 Double spheres

We calculated and analyzed the changes in the fringe patterns of DIs by two spheres of same d=3.0μm and RI values but different **C** as the center connecting vector. Direction of **C** is marked by its components along x-, y- and z-axis in integers and C(=|**C**|) gives the center-to-center distance. For C < d, the two spheres merge into one stretched along **C** and can be used to examine the dependence of DI patterns on morphological changes and ability to resolve small changes. To characterize the 2D STFT spectrum of DIs, we obtained f_s and M_{sm} from each $|S(f, \theta; z)|$ and use them as a compressed presentation of |S|. Different **C** vectors were used and the calculated DIs were analyzed by the 2D STFT method. In addition, C was varied with step sizes at 0.075μm for 0.15μm ≤ C ≤ 0.75 μm and 0.30μm for 0.9μm ≤ C ≤ 6.00μm. Fig. 4 presents some calculated I(y, z) of different **C** ranging from (100) along x-axis to (111) in cubic diagonal direction. A careful comparison reveals that the scatterers of two spheres exhibit observable changes in patterns among the six directions of **C** in terms of pattern orientation and shifts of bright and dark fringes when C becomes larger than 0.3μm, which is confirmed by the different patterns in each paired plots of f_s and M_{sm} in Fig. 5.

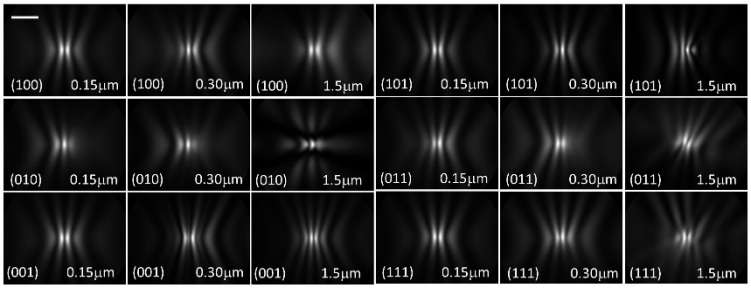

Fig. 4. Examples of calculated DIs of two spheres with d=3.0μm, bar=10°. The direction and magnitude of **C** are marked in each image. Other parameters are the same as those in Fig. 2.

After DI simulations, STFT analysis was performed to transform these images into the 2D space of f and θ with the line sampling angle θ varied from 0 to 179° with a step of 1°. To further compress the spectral data for efficient analysis, we reduced the θ dependence of sideband parameters f_s and M_{sm} for 180 angles to 36 angular bands of 5° width for each bands' centers, marked as θ_b, that ranges from 0 to 175°. The parameters were averaged over 3° for each θ_b to minimize fluctuation. Fig. 5 presents paired contour plots of $f_s(\theta_b, C)$ and $M_{sm}(\theta_b, C)$ with different **C**. One can clearly see that the DIs of double spheres produce distinct contour structures as C increases to above 0.30μm in the paired plots. Combined with the DIs shown in Fig. 4, these results indicate the resolving power of the diffraction imaging unit with λ=532nm should be less than 0.3μm or 300nm as a scatter is "stretched" in all six directions in 3D space.

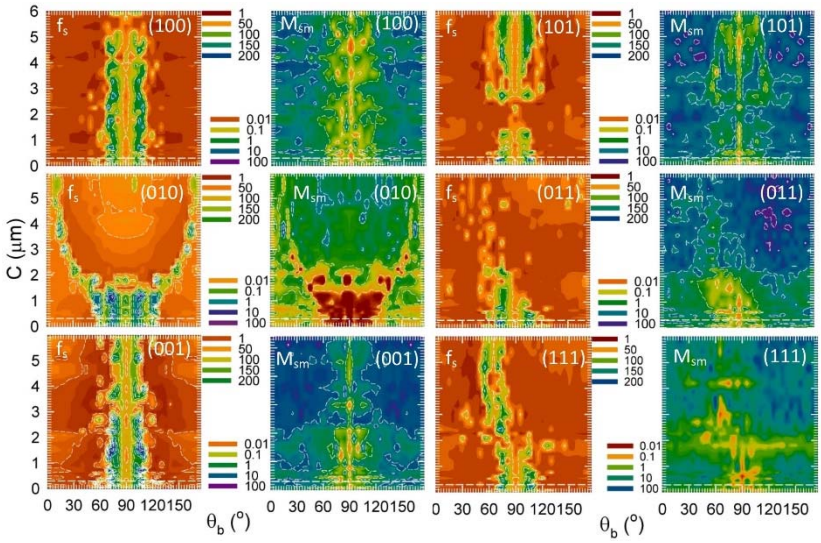

Fig. 5. The paired contour plots of $f_s(\theta_b, C)$ and $M_{sm}(\theta_b, C)$ obtained from calculated DIs of two spheres with d=3.0μm, 0.075μm ≤ C ≤ 6.0 μm and **C** directions as marked in each image. The white dash lines indicate C=0.30μm. Other parameters are the same as those in Fig. 2.

4. Discussions and Summary

The resolving power of DI for morphological variations in scatterers is poorly understood due to the complex relations between the changes and image features. The 2D STFT method described in this report provides a resource for such investigation. Analysis on DIs by single spheres clearly shows that the STFT sideband parameters cannot be used to distinguish small spheres of d=1 or 1.5μm. It should be pointed out that other image processing methods could be applied to extract pattern change among DIs by spheres of d < 2μm by, e.g., quantifying the size changes of the central bright spot. In contrast, the results with DIs of two spheres demonstrate the ability of DIs in 2D form to reflect a scatter's morphological changes in 3D space including the axial direction of imaging. Furthermore, each DI represented by a horizontal line in f_s or M_{sm} plot displays different angular variations (shown by colors) in Fig. 5 that could be used to detect small changes (stretched along 6 directions) in morphology. The results thus provide direct evidences that the objective based diffraction imaging has resolutions for morphological changes that are in par with the Abbe diffraction limit at about 0.5 μm on the lateral resolution of far-field imaging using conventional incoherent illumination and an objective of NA=0.55. We also performed additional study with two spheres replaced by equally sized cylinders and similar results were obtained. Even though the resolving power of DIFC is less than those of super-resolution microscopy methods [20], the combined advantages of DIFC make it a valuable tool for assay of small particles and cells in terms of label-free acquisition, simplicity in design, fast throughput and automated image processing.

In summary, we applied a validated a method of diffraction imaging simulation to calculate DIs and developed a 2D STFT method for analysis of resolving power for an imaging unit using objective of NA=0.55. The results show that the imaging unit can resolve morphological changes smaller than 300nm for a coherent illumination with wavelength at 532nm.